The Potential Roles of Background Surface Wind in the SST Variability Associated with Intraseasonal Oscillations

KAYA KANEMARU

Graduate School of Environmental Studies, Nagoya University, Nagoya, Japan

HIROHIKO MASUNAGA

Hydrospheric Atmospheric Research Center, Nagoya University, Nagoya, Japan

(Manuscript received 13 December 2013, in final form 13 June 2014)

ABSTRACT

The current study is aimed at exploring the potential roles of the seasonally altering background surface wind in the seasonality of the intraseasonal oscillations (ISOs) with a focus on the sea surface temperature (SST) variability. A composite analysis of the ocean mixed layer heat budget in term of ISO phases with various satellite data is performed for boreal winter and summer. The scalar wind is found to be a dominant factor that accounts for the ocean surface heat budget, implying that the background surface wind as well as its anomaly is important for the SST variability. An easterly anomaly to the east of convection diminishes scalar wind, and thus latent heat flux, when superposed onto a background westerly wind, implying that the presence of basic westerly wind is important for the development of a warm SST anomaly ahead of the ISO convection. On the other hand, an easterly anomaly in combination with basic easterly wind magnifies scalar wind and latent heat flux and cancels out the shortwave heat flux anomaly. The seasonal migration of the background westerly wind, which is confined to a southern equatorial belt in boreal winter but spread across the northern Indian Ocean in boreal summer, may offer a mechanism that partly accounts for the seasonal characteristics of ISO propagation. The northward propagation of the SST variability associated with the boreal summer ISO is found to also involve a similar mechanism with the meridional wind modulation of scalar wind.

1. Introduction

The intraseasonal oscillation (ISO; 30–90 days) is one of the dominant modes of atmospheric variability over the tropics (Madden and Julian 1971, 1972), and its behavior is seasonally changed (Madden 1986; Gutzler and Madden 1989; Wang and Rui 1990; Salby and Hendon 1994; Zhang and Dong 2004). The convective activity of the boreal winter ISO [also known as the Madden–Julian oscillation (MJO)] initiated in the Indian Ocean propagates eastward along the equator to the Maritime Continent, being slightly shifted southward as it eventually enters the South Pacific convergence zone (SPCZ) (e.g., Hendon and Liebmann 1990; Matthews et al. 1996; Wheeler and Hendon 2004). The convection associated with the boreal summer ISO (BSISO) moves northeastward from the Indian Ocean into the southeast Asian continent and northwestern Pacific (e.g., Yasunari 1979, 1980; Krishnamurti and Subrahmanyam 1982).

Evidence for the air–sea coupling related with the ISO variability has been observed in previous studies. A warm sea surface temperature (SST) anomaly propagates preceding the enhanced convection associated with the ISO (Nakazawa 1995; Hendon and Glick 1997; Shinoda et al. 1998; Woolnough et al. 2000), which arises from an enhancement of insolation and a weakening of evaporation. This relation between ISO propagation and the SST variability is observed in both the MJO (e.g., Lau and Sui 1997; Hendon and Glick 1997; Shinoda et al. 1998; Vialard et al. 2008) and BSISO (e.g., Kemball-Cook and Wang 2001; Sengupta et al. 2001; Klingaman et al. 2008), which implies that the SST variability has potential importance in the maintenance of ISO propagation. Some model studies suggest that the air–sea coupling affects the ISO propagation mechanism (e.g., Flatau et al. 1997; Wang and Xie 1998; Waliser et al. 1999; Kemball-Cook et al. 2002;

Corresponding author address: Kaya Kanemaru, Graduate School of Environmental Studies, Nagoya University, Furo-cho, Chikusa-ku, Nagoya 464-8601, Japan.
E-mail: kanemaru@satellite.hyarc.nagoya-u.ac.jp

DOI: 10.1175/JCLI-D-13-00774.1

Woolnough et al. 2007). The SST response associated with ISOs seasonally and regionally differs over the Indian Ocean and the western Pacific. Duvel and Vialard (2007) pointed out that the amplitude of the SST variability is related to the thickness of the climatological ocean mixed layer and the large SST variability is observed in the summer hemisphere. Li et al. (2008) also suggested that a large SST variability is involved in the phase relationship between shortwave heat flux and wind-driven latent heat flux depending on seasonal background winds. As such, surface heat flux anomalies associated with ISOs are important for explaining the ISO seasonality when superposed on the seasonally varying background wind. Meanwhile, the roles of seasonally altering background wind in the SST variability associated with ISO have not been extensively studied yet.

Figure 1 shows outgoing longwave radiation (OLR) and SST anomalies associated with ISO composited for each ISO phase by Wheeler and Hendon (2004). Details in the methodology of the composite analysis are described in section 2. A negative OLR anomaly (solid contours) as an index of the enhanced convective activity travels eastward over the Indian Ocean in the initial phases and subsequently shifts to southward (northward) in boreal winter (summer). Moreover, positive SST anomalies (color shaded) are found to precede the enhanced ISO convection in both boreal winter and summer. This confirms the existing knowledge that a warm SST anomaly emerges ahead of the ISO convection regardless of season, although the ISO propagation direction is largely different between the seasons. Inness and Slingo (2003) and Inness et al. (2003) pointed out that the improvement of basic surface westerly wind simulated by the air–sea coupling model results in a better representation of the ISO. A working hypothesis to examine in this study is that a seasonal contrast in the background surface wind may be a key factor that explains the SST variability associated with the ISO.

A global-scale observational dataset of a variety of parameters including surface heat fluxes, SST, and rainfall is of key importance for further understanding of air–sea interactions involved in the ISO (Hendon 2012). Reanalysis products provide an extremely useful dataset with continuous coverage in space and time at the expense of their dependence on model parameterizations. In situ observations offer accurate and frequent measurements while restricted to a limited spatial and temporal coverage. Satellites uniformly observe the entire globe, although the quality and variety of satellite retrievals may be limited by sensor capability. Recent advances in satellite remote sensing technology, however, have significantly improved the potential utility of satellite observations by means of an integrated use of satellite data. In this study, satellite observations are extensively exploited to understand the SST variability related to the ISO over the tropical Indian and Pacific Oceans. A seasonally independent ISO index proposed by Wheeler and Hendon (2004) is utilized to identify different ISO phases in boreal winter and summer.

The current study aims to explore the potential roles of the seasonally altering background surface wind in the seasonality of the ISOs with focus on the SST variability based on an ocean mixed layer heat budget analysis conducted with satellite data. The analysis method is introduced in section 2. The seasonality and regionalism of SST and heat flux changes are shown in section 3. A summary and discussion are presented in section 4.

2 Data and method

a. Ocean heat budget estimation

This study uses a variety of datasets based on satellite observations to analyze the ocean mixed layer heat budget associated with the ISO. The methodology is adopted from Masunaga and L'Ecuyer (2010, 2011) with some updates in the current study. The tendency equation of ocean mixed layer temperature (MLT) may be written as

$$\frac{\partial T_s}{\partial t} = \frac{Q_{\rm net}}{\rho_w C_{p,w} H_{\rm ml}} + \epsilon, \tag{1}$$

where T_s, $Q_{\rm net}$, ρ_w, $C_{p,w}$, $H_{\rm ml}$, and ϵ are SST, the net heat flux into the ocean mixed layer, the ocean water density ($1030\,{\rm kg\,m^{-2}}$), the specific heat of ocean water ($4.0 \times 10^3\,{\rm J\,kg^{-1}\,K^{-1}}$), the ocean mixed layer depth, and a residual term that contains currently ignored factors (e.g., entrainment cooling and vertical diffusion at the bottom of the ocean mixed layer) and retrieval error, respectively. The net heat flux $Q_{\rm net}$ is divided into

$$Q_{\rm net} = Q_{\rm SW} + Q_{\rm LW} + Q_{\rm LH} + Q_{\rm SH} + Q_{\rm upw} + Q_{\rm adv} + Q_{\rm dif}, \tag{2}$$

where $Q_{\rm SW}$ is the shortwave flux absorbed into the ocean mixed layer, $Q_{\rm LW}$ is the net longwave flux at the surface, $Q_{\rm LH}$ is the latent heat flux, $Q_{\rm SH}$ is the sensible heat flux, $Q_{\rm upw}$ is the heat flux by upwelling through the ocean mixed layer bottom, $Q_{\rm adv}$ is the heat flux transported by horizontal advection within the ocean mixed layer, and $Q_{\rm dif}$ is the horizontal diffusional heat flux. The input data sources are summarized in Fig. 2.

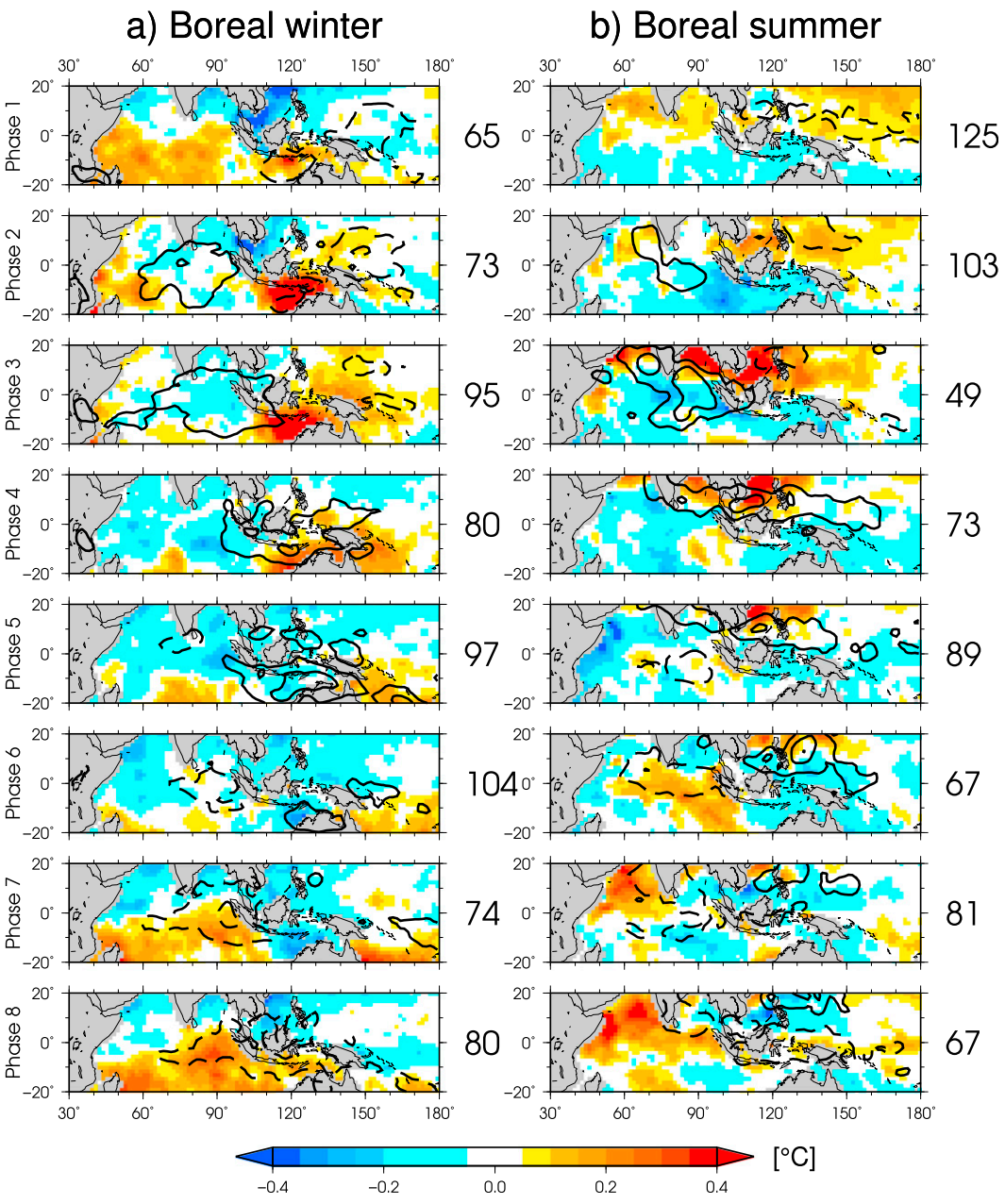

FIG. 1. OLR (contours) and SST (shaded) anomalies for each MJO phase by Wheeler and Hendon (2004) in (a) boreal winter and (b) boreal summer. Solid contours indicate −30 and −15 W m^{-2} and dashed contours indicate 15 and 30 W m^{-2}. The number of days averaged within each phase is shown on the right of each panel. Maps are smoothed by a 4.5° × 4.5° moving average.

The downwelling surface shortwave radiation (SSR) flux $F^{\downarrow}_{\mathrm{SW}}$ and surface longwave radiation (SLR) flux $F^{\downarrow}_{\mathrm{LW}}$ are provided by the Hydrologic Cycle and Earth Radiation Budget (HERB) algorithm, where radiative fluxes are estimated from cloud and precipitation properties observed from Tropical Rainfall Measuring Mission (TRMM) Microwave Imager (TMI) and TRMM Visible and Infrared Scanner (VIRS) (L'Ecuyer and Stephens 2003; L'Ecuyer and McGarragh 2010). The net shortwave heat flux absorbed into the ocean mixed layer is

$$Q_{\mathrm{SW}} = (1-\alpha)\Pi F^{\downarrow}_{\mathrm{SW}}, \tag{3}$$

where α and Π are the ocean albedo of 0.07 (Morel and Antoine 1994) and the fraction of incoming shortwave

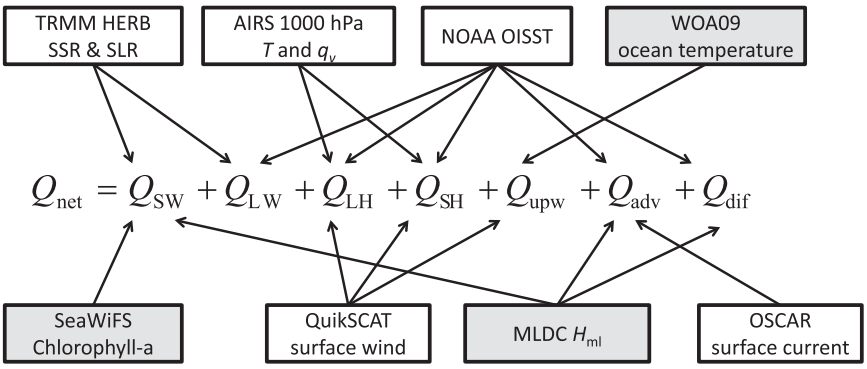

FIG. 2. Data sources for each heat flux estimate. Gray shaded boxes indicate climatological data instead of time series. Details are given in the text.

radiation absorbed by the ocean mixed layer, respectively. In this study, Π is estimated as

$$\Pi = 1 - 0.57\left[V_1 \exp\left(-\frac{H_{\rm ml}}{Z_1}\right) + V_2 \exp\left(-\frac{H_{\rm ml}}{Z_2}\right)\right], \quad (4)$$

where V_1, V_2, Z_1, and Z_2 are determined for a given chlorophyll-*a* concentration (Table 2 of Morel and Antoine 1994). The chlorophyll-*a* concentration is obtained from the level 3 standard mapped image product of the Sea-viewing Wide Field-of-view Sensor (SeaWiFS) on board the *OrbView-2* satellite (O'Reilly et al. 2000) and provided by the National Aeronautics and Space Administration (NASA) ocean color website. This study uses $H_{\rm ml}$ given as the density-based mixed layer depth taken from mixed layer depth climatology (MLDC; de Boyer Montégut et al. 2004).

The net longwave heat flux at the surface is written as

$$Q_{\rm LW} = F^{\downarrow}_{\rm LW} - \sigma T_s^4, \quad (5)$$

where σ is the Stephan–Boltzmann constant ($5.67 \times 10^{-8}\,{\rm W\,m^{-2}\,K^{-4}}$) and T_s is SST obtained from the National Oceanic and Atmospheric Administration (NOAA) daily optimum interpolation SST (OISST) version 2 (Reynolds et al. 2007). The OISST dataset is derived from in situ data and Advanced Very High Resolution Radiometer (AVHRR) and Advanced Microwave Scanning Radiometer for Earth Observing System (AMSR-E) measurements.

The sensible heat and latent heat fluxes from the ocean surface are calculated from the bulk method,

$$Q_{\rm SH} = -C_p \rho_a C_\theta |\mathbf{u}_{10}|(T_s - T_a) \quad \text{and} \quad (6)$$

$$Q_{\rm LH} = -L_v \rho_a C_E |\mathbf{u}_{10}|[q_v^*(T_s) - q_{v,s}], \quad (7)$$

where C_p, ρ_a, $\mathbf{u}_{10}$, T_a, L_v, $q_v^*(T_s)$, and $q_{v,s}$ are the specific heat of dry air at constant pressure ($1004\,{\rm J\,kg^{-1}\,K^{-1}}$), the density of dry air ($1.2\,{\rm kg\,m^{-3}}$), the wind vector at 10 m above ocean surface, the surface air temperature, the latent heat of vaporization ($2.5 \times 10^6\,{\rm J\,kg^{-1}\,K^{-1}}$), the saturation water vapor mixing ratio at T_s, and the surface water vapor mixing ratio, respectively. The bulk transfer coefficients C_θ and C_E parameterized as a function of $|\mathbf{u}_{10}|$ are adopted from Eqs. (A1a)–(A1c) of Large et al. (1994). In this study, T_a and $q_{v,s}$ are estimated from a logarithmic vertical profile within the simple surface layer (SL) model by Kanemaru and Masunaga (2013),

$$\theta_s = \theta_{\rm ML} + \frac{\ln(z/z_{\rm SL})}{\ln(z_\theta/z_{\rm SL})}[\theta(p_s, T_s) - \theta_{\rm ML}] \quad \text{and} \quad (8)$$

$$q_{v,s} = q_{v,{\rm ML}} + \frac{\ln(z/z_{\rm SL})}{\ln(z_q/z_{\rm SL})}[q_v^*(T_s) - q_{v,{\rm ML}}], \quad (9)$$

where $\theta_{\rm ML}$, $q_{v,{\rm ML}}$, $\theta(p_s, T_s)$, and z are the atmospheric mixed layer (ML) potential temperature, the ML water vapor mixing ratio, the potential temperature for T_s and surface pressure p_s, and the observation height, respectively. The *Aqua* level 2 Advanced Microwave Sounder Unit (AMSU) and Atmospheric Infrared Sounder (AIRS) combined retrieval (AIRX2RET; hereafter simply AIRX) version 6 product (Susskind et al. 2003, 2011) contains p_s and air temperature T and water vapor mixing ratio q_v at the 1000-hPa level. In this study, $\theta_{\rm ML}$ and $q_{v,{\rm ML}}$ are defined at 1000 hPa. Surface potential temperature θ_s is converted to

$$T_a = \theta_s \left(\frac{p_s}{1000}\right)^{R_d/C_p}, \quad (10)$$

where R_d is the gas constant for dry air ($287\,{\rm J\,K^{-1}\,kg^{-1}}$). The roughness lengths for temperature z_θ and moisture z_q are given by the empirical coefficients of Large et al. (1994),

$$z_\theta = \begin{cases} 10\exp\left(-\dfrac{10^3}{32.7}\kappa\right), & \text{if} \quad T_s \geq T_a \\ 10\exp\left(-\dfrac{10^3}{18.0}\kappa\right), & \text{if} \quad T_s < T_a \end{cases} \quad \text{and} \tag{11}$$

$$z_q = 10\exp\left(-\frac{10^3}{34.6}\kappa\right), \tag{12}$$

where κ is the von Kármán constant (0.40). It is assumed in this study that $z_{SL} = 50\,\text{m}$ and $z = 3\,\text{m}$. The AIRX product also contains T_a and $q_{v,s}$, which are compared to in situ observations and shown in the appendix. The Quick Scatterometer (QuikSCAT) SeaWinds version 4 product (Ricciardulli and Wentz 2011) provided by Remote Sensing Systems contains $\mathbf{u}_{10}$ over the ocean surface.

The upwelling heat flux is evaluated as

$$Q_{\text{upw}} = -\rho_w C_{p,w} w_E \mathcal{H}(w_E)\Delta T_E, \tag{13}$$

where $\mathcal{H}$ and ΔT_E are the Heaviside function and the temperature difference between ocean mixed layer water and upwelling water, respectively. The upwelling velocity w_E is estimated as

$$w_E = \frac{1}{\rho_w}\nabla \cdot \mathbf{M}_E. \tag{14}$$

The Ekman mass transport $\mathbf{M}_E$ is evaluated from

$$r_s M_{E,x} - f M_{E,y} = \tau_x = \rho_a C_D |\mathbf{u}_{10}| u_{10} \quad \text{and} \tag{15}$$

$$r_s M_{E,y} + f M_{E,x} = \tau_y = \rho_a C_D |\mathbf{u}_{10}| v_{10}, \tag{16}$$

where r_s is the drag coefficient, f is the Coriolis parameter, $M_{E,x}$ and $M_{E,y}$ are the zonal and meridional component of the Ekman mass transport, τ_x and τ_y are the zonal and meridional wind stresses, C_D is the bulk transfer coefficient obtained by Eq. (A1a) in Large et al. (1994), and u_{10} and v_{10} are the zonal and meridional winds at 10 m above ocean surface. In the current study, r_s is $6.62 \times 10^{-6}\,\text{s}^{-1}$ (Lagerloef et al. 1999). From previous studies, ΔT_E is estimated as the difference between ocean temperature at the ocean mixed layer and either 10 m (Foltz et al. 2010; Drushka et al. 2012) or 20 m (Chang 1993; Wang and McPhaden 1999) below the ocean mixed layer over the equatorial Indian and Pacific Oceans. In the current study, the estimate of ΔT_E is adopted from Masunaga and L'Ecuyer (2010, 2011) as the difference between the depth of 0.5 H_{ml} and H_{ml} + 15 m using the *World Ocean Atlas 2009* (*WOA09*) temperature profile (Locarnini et al. 2010).

TABLE 1. Data product resolutions.

Product	Spatial resolution	Temporal resolution
SeaWiFS	$1/12° \times 1/12°$	Climatology
OISST	$0.25° \times 0.25°$	1 day
QuikSCAT	$0.25° \times 0.25°$	1 day
HERB	$0.25° \times 0.25°$	1 day
OSCAR	$1° \times 1°$	5 day
WOA09	$1° \times 1°$	Climatology
MLDC	$2° \times 2°$	Climatology
AIRX	50-km footprint	1 day

The horizontal advection heat flux is evaluated as

$$Q_{\text{adv}} = -C_{p,w}\rho_w H_{\text{ml}} \mathbf{u} \cdot \nabla T_s, \tag{17}$$

where $\mathbf{u}$ is the current velocity within the ocean mixed layer. The Ocean Surface Current Analysis–Real Time (OSCAR) product (Bonjean and Lagerloef 2002) contains the near-surface current over the 0–30-m layer mean. This study adopts it as is for the ocean mixed layer current.

The horizontal diffusion heat flux is written as

$$Q_{\text{dif}} = C_{p,w}\rho_w H_{\text{ml}} \kappa_h \nabla^2 T_s, \tag{18}$$

where the turbulent diffusion coefficient κ_h is $3 \times 10^3\,\text{m}\,\text{s}^{-1}$ (Bauer et al. 1998).

b. *Data preprocessing*

The satellite products have various spatial resolutions as shown in Table 1. The AIRX product contains swath data of about 50-km spatial resolution at nadir corresponding to an AMSU-A footprint with an AIRS 3×3 array with cloud contamination algorithmically cleared. Other products are provided as gridded data. All the datasets are projected onto a common $1.5° \times 1.5°$ gridded data. In this study, analyzed data have daily temporal resolution except for the climatological parameters provided by *WOA09*, SeaWiFS, and MLDC products. The OSCAR product with a 5-day resolution is temporally interpolated to daily data. Ascending and descending orbits in AIRX and QuikSCAT products are averaged together into daily data. The SSR flux of the HERB algorithm is diurnally averaged (L'Ecuyer and McGarragh 2010). The SST tendency of (1) is calculated by a central difference of daily OISST data.

Data are sampled only where TRMM HERB, AIRX, and QuikSCAT measurements are available. AIRX and QuikSCAT estimates are affected by rain and clouds. The AIRX data are interpolated from the neighboring eight grid pixels averaged together to fill data gaps due to clouds and rain. This interpolation decreases sampling bias, although the accuracy of satellite estimates is

degraded (Kanemaru and Masunaga 2013). We also use OLR derived by the AIRX product as a proxy of deep convection and QuikSCAT surface wind vector data. In the current study, the 81-day running mean is subtracted from all the data. If the 81-day running mean is subtracted, both the seasonal cycle and longer-time scale variability are removed from the data.

c. ISO composite

A composite analysis is performed to reveal the propagation characteristics of the ISO. In the current study, the real-time multivariate MJO (RMM) index proposed by Wheeler and Hendon (2004) is used. This index is independent of season and defined from the first two empirical orthogonal functions of the combined fields of OLR and zonal winds at 850 and 200 hPa meridionally averaged between 15°S and 15°N. Eight MJO phases are defined based on a pair of the normalized principal components (RMM1 and RMM2) and the MJO intensity is given by their amplitude of $(\mathrm{RMM1}^2 + \mathrm{RMM2}^2)^{1/2}$. The current study analyzes only days when the amplitude normalized by their climatological standard deviation is greater than 1. Composites in boreal winter (November–March) and boreal summer (May–September) are individually analyzed to study the seasonality of SST changes associated with the ISO.

3. Results

a. OLR and SST

Composite analysis results in boreal winter and summer are presented in this section to reveal the seasonality and regionalism of convection and SST changes associated with ISOs. The composite result shown in Fig. 1 has been already presented in section 1, but the result is further examined. In boreal winter (Fig. 1a), a positive OLR anomaly (dashed contours) is located over the Maritime Continent and the western Pacific in phases 8 and 1; that is, these phases correspond to the suppressed convection stage of the MJO. A negative OLR anomaly or enhanced convection (solid contours) is initiated over the equatorial Indian Ocean in phase 2 and moves eastward in the subsequent phases. In phases 4 and 5, the negative OLR anomaly continues to propagate eastward but begins shifting slightly southward from the equator to northern Australia. In phases 6 and 7, the convection decays as it reaches the western Pacific, while a suppressed convection begins to develop over the Indian Ocean. In boreal summer (Fig. 1b), an active convection anomaly in the beginning of the BSISO is located over the equatorial Indian Ocean in phase 2 and extended to the northeast side in phase 3. In phases 4 and 5, the negative OLR anomaly propagates northeastward extensively from the Bay of Bengal to the western Pacific. A suppressed convection over the Indian Ocean appears the southwest of the negative OLR anomaly and propagates northeastward in phases 6–8. Over the western Pacific, the negative OLR anomaly remains stationary or propagates northward rather than eastward. The propagation characteristics of ISOs shown in Fig. 1 agree with known ISO modes such as the eastward propagating mode in boreal winter, the northeastward propagating mode over the Indian Ocean, and the northward propagating mode over the western Pacific in boreal summer (Wang and Rui 1990).

An SST anomaly (color shaded in Fig. 1) is also found to overall propagate eastward but precede the ISO convection described above. In boreal winter, a warm SST anomaly is found to emerge before the MJO convection develops over the Indian Ocean (phases 7, 8, and 1) and the channel north of Australia (phases 2 and 3). In boreal summer, a positive SST anomaly preceding the enhanced convection associated with the BSISO is located over the equatorial Indian Ocean and the Arabian Sea (phases 8 and 1) and the Bay of Bengal (phases 3 and 4). The first four phases show clear evidence that SST leads convection as the ISO proceeds, while the relationship between OLR and SST is unclear in the next four phases.

Latitudes with prominent SST variability are seasonally different. In phase 1, for example, positive SST anomalies are located over the Southern (Northern) Hemisphere in boreal winter (summer), so that a warm SST anomaly is shifted to the summer hemisphere. The SST variability over the summer hemisphere is larger than the winter hemisphere (Duvel and Vialard 2007; Li et al. 2008). Given that the seasonal cycle has been removed by subtracting the 81-day running mean in the current study, the meridional migration of SST is not mere a seasonal march but should be a property intrinsic to ISO propagation.

b. Heat fluxes

The origins of the SST variability are investigated by the ocean mixed layer heat budget introduced in section 2 and compared with heat fluxes divided into the seven components in (2). Figure 3 shows each heat flux anomaly in phase 2 of boreal winter. The variations of Q_{SW} and Q_{LH} have a dominant contribution over other fluxes to the heat budget. The spatial distribution of Q_{SW} anomaly closely resembles the OLR anomaly pattern, which suggests that Q_{SW} is modulated mostly by the surface insolation strongly reflecting the variability of high cloud amount. The other heat fluxes except for Q_{SW} and Q_{LH} have no appreciable contribution. These

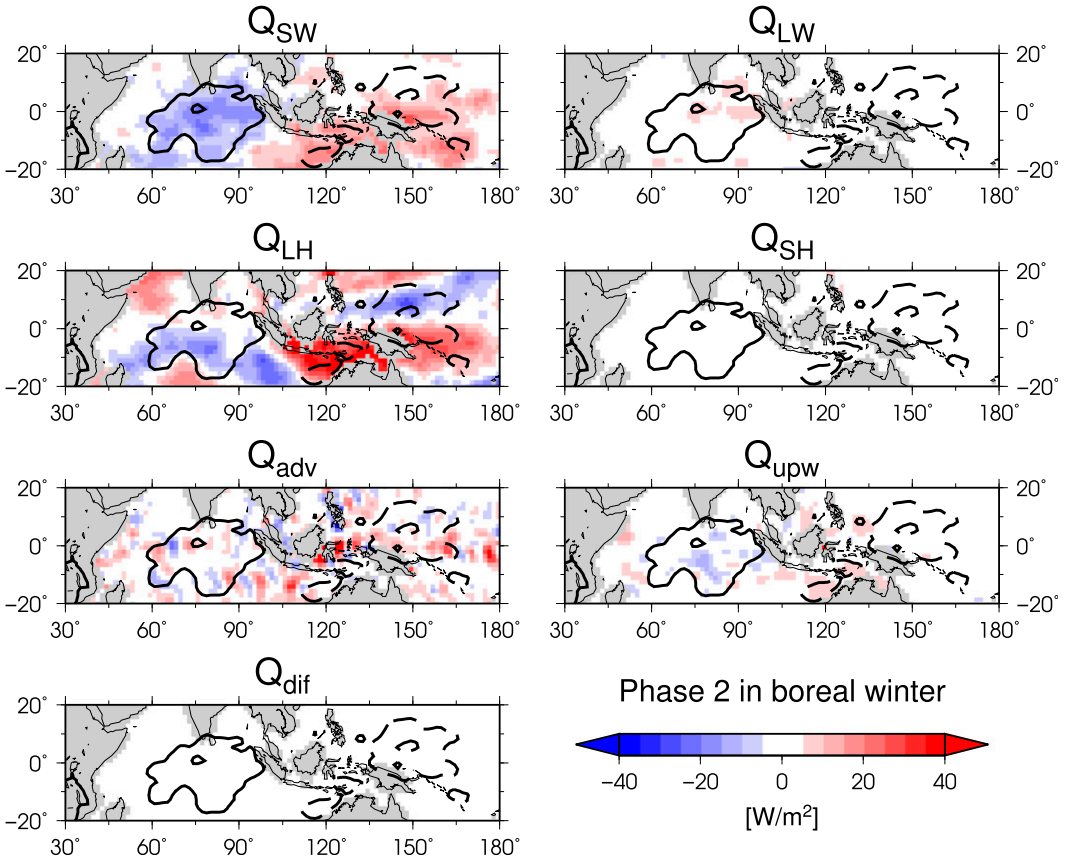

FIG. 3. As in Fig. 1a, but for heat flux breakdown of phase 2.

results are also shown in other ISO phases and the other season (not shown). The ocean mixed layer heat budget is mainly controlled by the variations of Q_{SW} and Q_{LH}, which is consistent with the known observational characteristics in boreal winter (e.g., Lau and Sui 1997; Hendon and Glick 1997; Shinoda et al. 1998; Vialard et al. 2008) and summer (e.g., Kemball-Cook and Wang 2001; Sengupta et al. 2001; Klingaman et al. 2008).

The variation of Q_{SW} is mostly explained by the propagation of cloud systems associated with the ISO. The variation of Q_{LH} is not as easy to interpret because Q_{LH} is a function of scalar wind and moisture deficit shown in (7). The total derivative of logarithmic transformation of (7) is

$$\frac{dQ_{\mathrm{LH}}}{Q_{\mathrm{LH}}} = \frac{dU}{U} + \frac{dC_E}{C_E} + \frac{d\Delta q_v}{\Delta q_v}, \tag{19}$$

where U is $|\mathbf{u}_{10}|$ and Δq_v is the moisture deficit or $q_v^*(T_s) - q_{v,s}$. In the current study, C_E is adopted from Large et al. (1994) as a function of U so the C_E term is integrated into the U term:

$$\frac{dQ_{\mathrm{LH}}}{Q_{\mathrm{LH}}} = \frac{dU}{U} + \frac{dU}{C_E}\frac{dC_E}{dU} + \frac{d\Delta q_v}{\Delta q_v} = \left(1 + \frac{U}{C_E}\frac{dC_E}{dU}\right)\frac{dU}{U} + \frac{d\Delta q_v}{\Delta q_v}. \tag{20}$$

Equation (20) is applied to the estimation of the anomaly (prime) from the temporal average (overbar) as

$$Q'_{\mathrm{LH}} = \left[1 + \frac{\overline{U}}{\overline{C_E}}\overline{\left(\frac{dC_E}{dU}\right)}\right]\overline{\frac{Q_{\mathrm{LH}}}{U}}U' + \overline{\frac{Q_{\mathrm{LH}}}{\Delta q_v}}\Delta q'_v. \tag{21}$$

The first and second terms on the right-hand side are the contribution of U and Δq_v, respectively. Figure 4 shows the decomposition of the Q_{LH} variability shown in Fig. 3. The variation of Q_{LH} primarily reflects the scalar wind variability, while the contribution of the moisture deficit and the residual term is relatively small.

c. Latitudinal difference in wind speed variability

Scalar wind is explained by the square root of the quadratic sum of zonal and meridional winds. The same zonal wind anomaly could enhance or diminish scalar

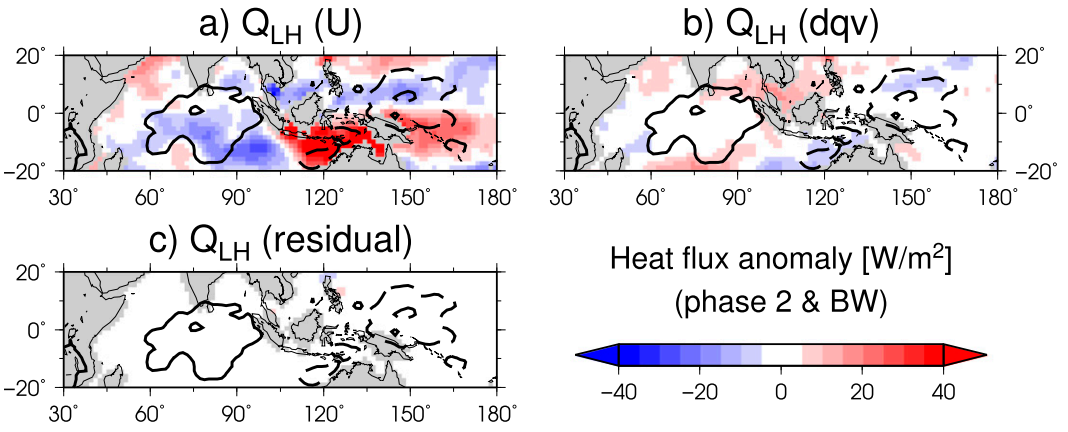

FIG. 4. As in Fig. 3, but for each term of Q_{LH} shown in (21): (a) the first term for U', (b) the second term for $\Delta q_v'$, and (c) the residual term.

wind when added onto the background wind, depending whether the anomalous wind direction is the same as or opposite to the background wind direction. Figure 5 shows the seasonal climatology of zonal wind in boreal winter and summer. In boreal winter (Fig. 5a), the easterly trade wind is dominant away from the equator, while the westerly wind dominates a southern equatorial band (10°S–0°) extending from the Indian Ocean to the western Pacific and northwest Australia. In boreal summer (Fig. 5b), the westerly wind spreads across the northern Indian Ocean to the western Pacific, and the easterly wind dominates the rest of the tropical ocean including the whole Southern Hemisphere and the central Pacific.

The influence of background wind direction on zonal and scalar wind anomalies is illustrated by contrasting two latitudinal bands of a northern band (NB; 3°–9°N) and a southern band (SB; 9°–3°S). The background wind direction is opposite between NB and SB for each season. Figure 6 shows the ISO phase versus longitude cross

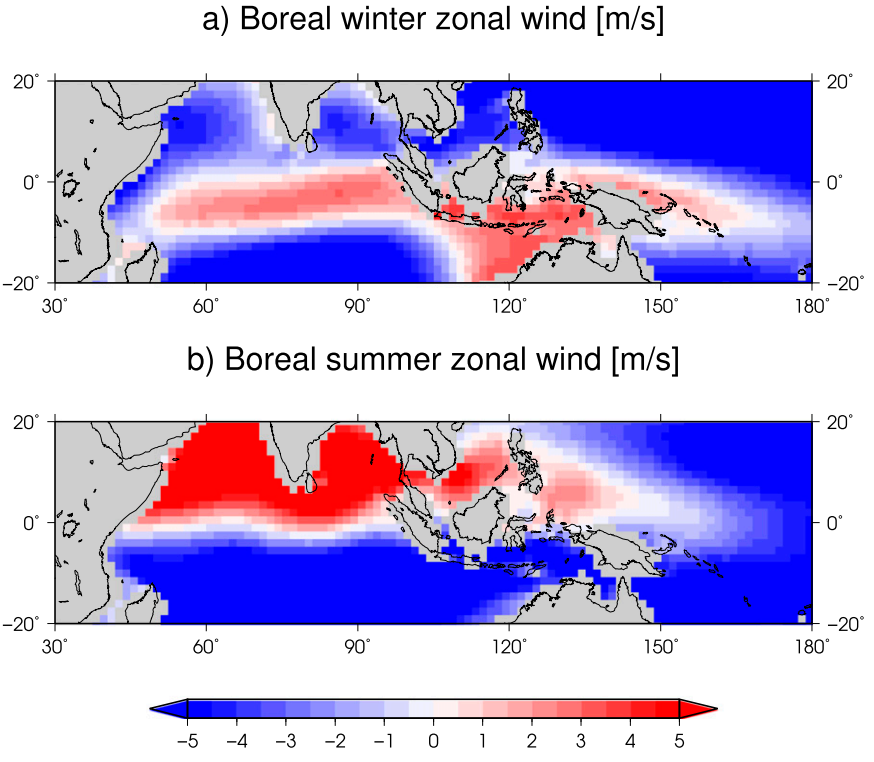

FIG. 5. Climatology of surface zonal wind in (a) boreal winter and (b) boreal summer.

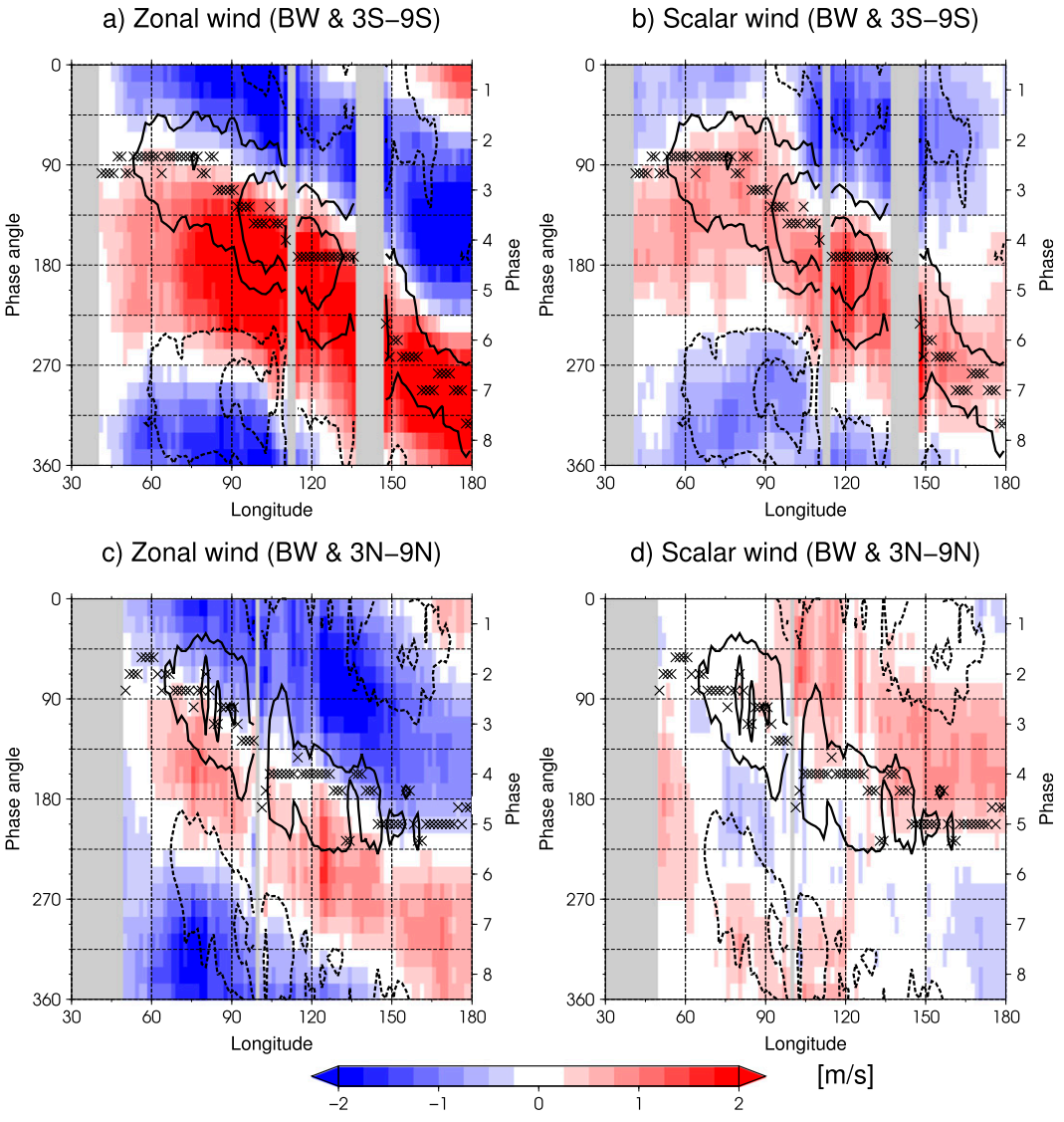

FIG. 6. ISO phase vs longitude section for the latitudinal bands SB (3°–9°S) and NB (3°–9°N) in boreal winter for (a),(c) zonal and (b),(d) scalar wind. The ISO phase is temporally smoothed by 105° (15° × 7) angle running mean. Solid contours indicate OLR of −20 and −10 W m^{-2} and dashed contours indicate OLR of 10 and 20 W m^{-2}. The landmass is indicated by gray shading. Crosses indicate the OLR minimum for each longitude.

section of zonal and scalar wind anomalies in boreal winter for each NB and SB. Zonal wind anomalies have an easterly (westerly) anomaly to the east (west) of the MJO convection, while scalar wind anomalies exhibit different behaviors between the NB and SB. In the SB where the basic wind is westerly in this season, scalar wind anomalies propagate eastward nearly in phase with zonal wind anomalies, and easterly (westerly) anomalies decrease (increase) scalar wind on the front (back) side of the propagating convection. In the NB where the basic wind is easterly, on the contrary, easterly anomalies slightly increase scalar wind ahead of the enhanced convection although the signal is weaker than in the SB. The scalar wind patterns are hence reversed between the NB and SB because of the difference in basic zonal wind (Fig. 5a).

To more clearly illustrate the regional difference, the composite plot is next sorted by the ISO phase angle relative to the convection peak (Fig. 7). Parameters shown in Fig. 6 are composited with respect to the OLR minimum at each longitude and then averaged together between 75° and 120°E. Easterly (westerly) anomalies in zonal wind are well captured before (after) the convection peak regardless of the areas studied (Fig. 7a). It is also evident, on the other hand, that scalar wind anomalies are largely different in phase between the NB

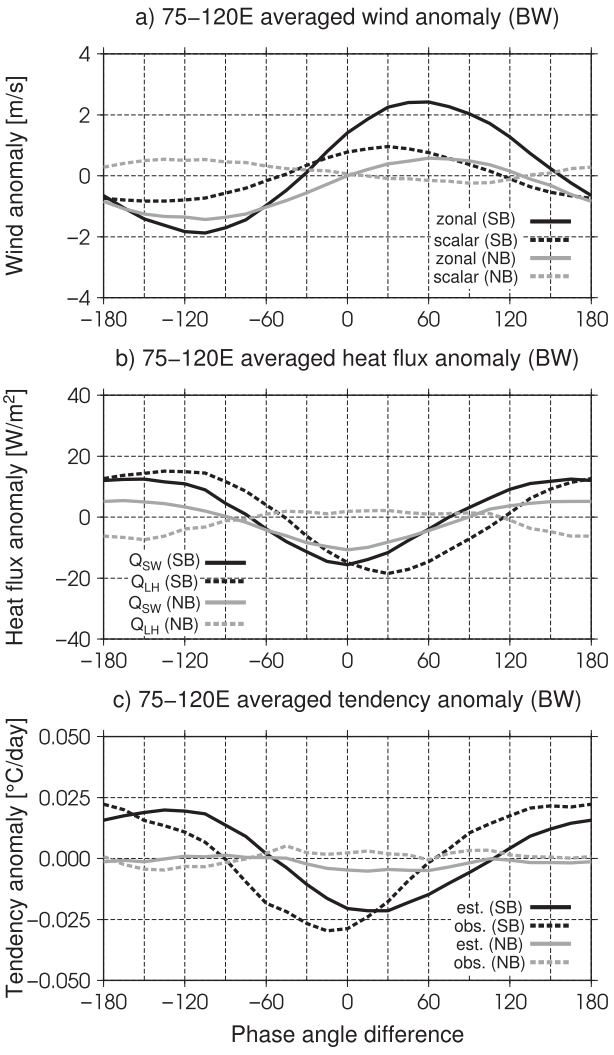

FIG. 7. Time series in terms of ISO phase angle relative to the OLR minimum for longitudinal average between 75° and 120°E in boreal winter for (a) zonal wind (solid) and scalar wind (dashed), (b) Q_{SW} (solid) and Q_{LH} (dashed), and (c) tendency of the estimated ocean MLT (solid) and observed SST (dashed). Black (gray) lines indicate the average in SB (NB).

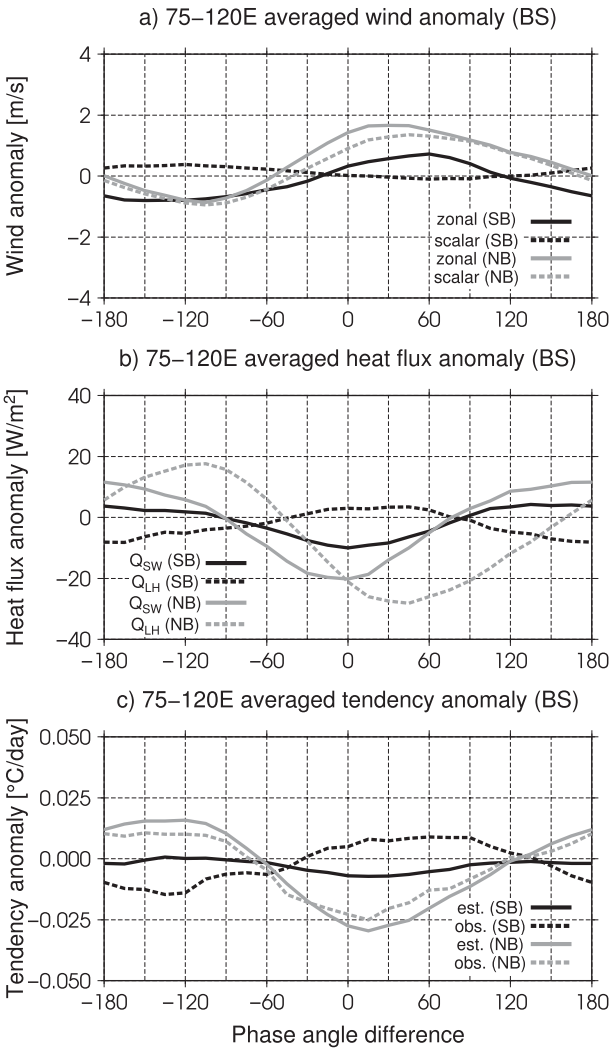

FIG. 8. As in Fig. 7, but for boreal summer.

and SB. The scalar wind anomaly is a key factor that accounts for the Q_{LH} variability shown in Fig. 4. Figure 7b shows the composite time series of Q_{SW} and Q_{LH}. Anomalies of Q_{SW} in both the NB and SB have negative anomalies in the enhanced convective stage (0° phase angle difference) and positive anomalies in the suppressed convection stage (±180°). In contrast, Q_{LH} changes its behavior between the areas. In the NB, the Q_{LH} variability is nearly 180° out of phase with Q_{SW} and therefore Q_{SW} and Q_{LH} cancel out each other, making the SST tendency extremely small (Fig. 7c). In the SB, on the other hand, the Q_{LH} anomaly changes in phase with the Q_{SW} anomaly, so that the Q_{LH} and Q_{SW} anomalies in tandem lead to a significant variation in the mixed layer heat budget that gives rise to an SST warming prior to the MJO convection. It is suggested that the background westerly wind is an important factor that drives the SST warming before the active MJO convection.

The background wind direction is an important factor also in boreal summer, while the SST variability characteristics are quite different from boreal winter. Figure 8 is the same as Fig. 7, but for boreal summer. Zonal wind anomalies are, similarly to the boreal winter case, in general easterly (westerly) preceding (following) negative OLR anomalies in both the NB and SB (Fig. 8a). Scalar wind anomalies have a negative peak in the NB and a subtle positive peak in the SB before the OLR minimum occurs, opposite to the boreal winter case. The contrasting behaviors between the different seasons are explained by the fact that basic zonal wind between the

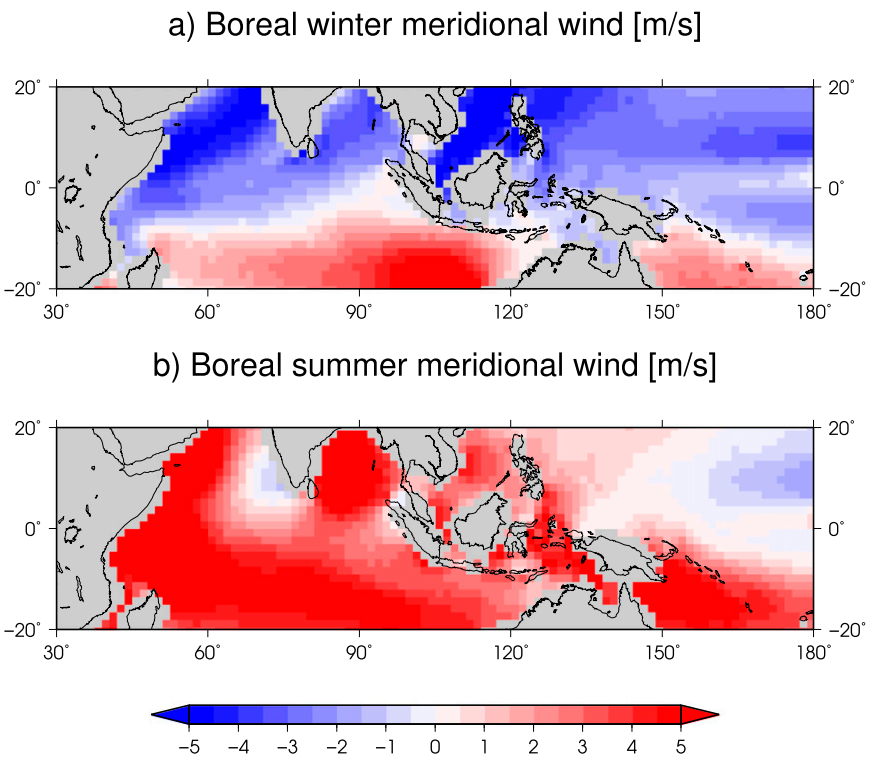

FIG. 9. As in Fig. 5, but for meridional wind.

NB and SB are seasonally reversed as seen in Fig. 5b. In the NB, although the Q_{LH} anomaly lags the Q_{SW} anomaly by about ¼ cycle (Fig. 8b), Q_{SW} and Q_{LH} work together rather than against each other to give rise to a distinct SST variation (Fig. 8c). In the SB, on the other hand, Q_{SW} and Q_{LH} are out of phase and cancel each other out to some extent, resulting in a relatively weak SST variability (Fig. 8c). The latitudinal difference of the phase relationship between Q_{SW} and Q_{LH} is consistent with Li et al. (2008) using reanalysis data. The variability of the estimated ocean MLT tendency agrees with the observed SST tendency in the NB (Fig. 8c), whereas it fails to agree in the SB. The disagreement may have arisen from the ignored heat fluxes and/or uncertainty in the heat budget analysis.

d. Meridional propagation in boreal summer

The BSISO and the SST variability are known to have a northward component of propagation over the Indian Ocean (Kemball-Cook and Wang 2001; Sengupta et al. 2001; Klingaman et al. 2008). The possibility is explored next that meridional wind may have a similar mechanism as found for zonal wind that facilitates the northward propagation of SST as well as the eastward migration. Figure 9 shows the seasonal climatology of meridional wind in boreal winter and summer. In boreal winter (Fig. 9a), the basic meridional wind is northerly north of 10°S and southerly south of 10°S from the Indian Ocean to the western Pacific. In boreal summer (Fig. 9b), on the other hand, the Eastern Hemisphere is dominated by southerlies except in the southwest of the Indian subcontinent and in the northern central Pacific. The ISO phase versus latitude diagrams of zonal, meridional, and scalar wind anomalies are shown in Fig. 10 and present the northward propagating BSISO over the Bay of Bengal with longitudes averaged between 84° and 96°E. Wind anomalies and OLR minima move northward from the equator and to the north as the BSISO proceeds. An easterly (westerly) anomaly precedes (lags) the OLR minimum (Fig. 10a). Moreover, meridional wind anomalies in the Northern Hemisphere are northerly (southerly), slightly leading (lagging) the OLR minimum (Fig. 10b). The basic meridional wind in boreal summer is entirely southerly over the Indian Ocean, so that the northerly (southerly) anomaly decreases (increases) scalar wind (Fig. 10c) in collaboration with anomalous zonal wind being enhanced or diminished when projected on to the background field. Figure 11, similar to Figs. 7 and 8, shows the composite time series in terms of the ISO phase angle relative to the OLR minimum latitudinally averaged between 3° and 18°N. Northerly and easterly anomalies precede the convective peak in phase with scalar wind. As a result, although the Q_{SW} anomaly is about 60° ahead of the

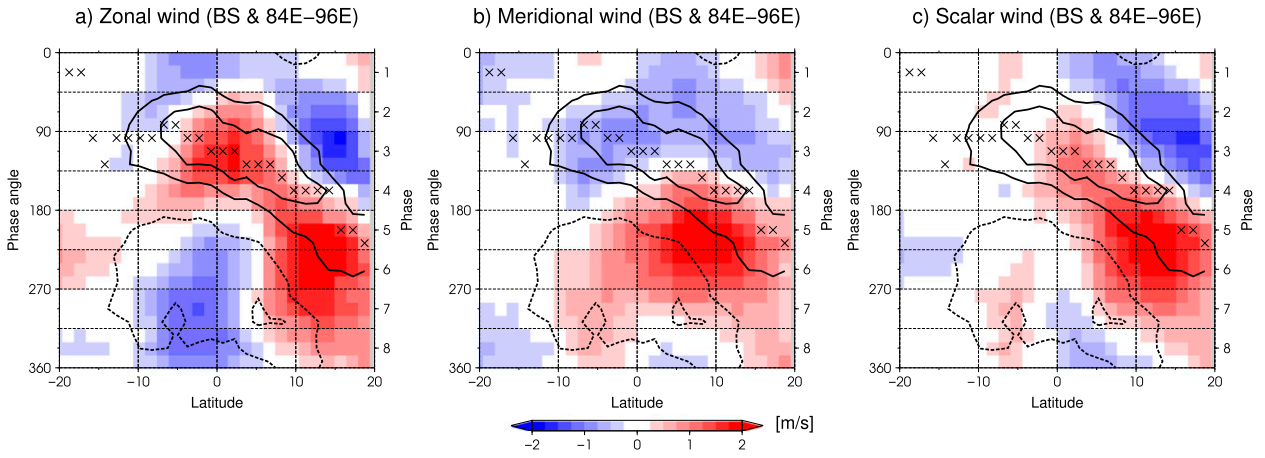

FIG. 10. As in Fig. 6, except for ISO phase vs latitude section for the longitudinal band between 84° and 96°E in boreal summer for (a) zonal wind, (b) meridional wind, and (c) scalar wind.

Q_{LH} anomaly, both anomalies enhance together during the convectively enhanced (suppressed) stage with negative (positive) anomalies (Fig. 11b). The estimated tendency of the ocean MLT agrees with the observed SST tendency (Fig. 11c). From the findings above, it is not only zonal wind but also meridional wind that has an important role in the preceding SST variability associated with the BSISO.

4. Summary and discussion

The current study aims to explore the potential roles of the seasonally altering background surface wind in the seasonality of the ISOs with a focus on the SST variability based on an observational data analysis. The analysis is performed with a variety of satellite data for the 7 years from November 2002 to September 2009. To examine the seasonal variation of ISO propagation, OLR, SST, surface heat fluxes, and ocean surface winds are composited in terms of ISO phases for each season of boreal winter (November–March) and summer (May–September).

Composite analysis results are found to reproduce the eastward propagation of the MJO shifting slightly to the south as it proceeds and the northeastward movement of the BSISO. The seasonal difference in ISO propagation agrees with the propagation characteristics of ISOs as reported in the literature (Wang and Rui 1990). The propagation of a warm SST anomaly preceding the enhanced ISO convection from the Indian Ocean to the Maritime Continent mainly arises from the variability of shortwave and latent heat fluxes. The shortwave flux variability is primarily explained by the movement of cloud systems blocking the incoming solar radiation, while the scalar wind variation is largely responsible for the modulation of the latent heat flux. The contribution of moisture deficit for the latent heat flux variability is small. Zonal wind anomalies are enhanced or diminished when superimposed onto the background field and this has a notable consequence on scalar wind anomaly. As a result, the geographical distribution of basic wind is important for latent heat anomalies and thus preceding SST variability involved in the ISO. In boreal winter, a basic westerly wind dominates a latitudinal band between 10°S and the equator, whereas an easterly anomaly to the east of the MJO decreases scalar wind and latent heat flux. The reduced latent heat flux precedes the enhanced convection stage and tends to warm SST there nearly in phase with the shortwave flux variation. Outside this narrow band of background westerlies, on the other hand, an easterly anomaly in combination with a basic easterly wind magnifies scalar wind and the latent heat flux, counteracting a concurrent positive shortwave flux anomaly.

In boreal summer, a basic westerly wind is located over the Northern Hemisphere, and the eastward propagation of the BSISO is found in the Northern Hemisphere in contrast with the boreal winter MJO. The relationship between northward propagation of the BSISO and the SST variability is related to not only the zonal wind but also the meridional wind. A northerly wind anomaly in the north of the active BSISO convection occurs in the region with background southerly and thus promotes SST warming, working together with the effect by anomalous zonal wind as described above.

Some previous studies have addressed the roles of the warm SST anomaly in the possible mechanisms of ISO propagation. Flatau et al. (1997) showed that a simulation forced with an empirical relationship between SST tendency and zonal wind on an aquaplanet produces more organized and slower propagation. They proposed

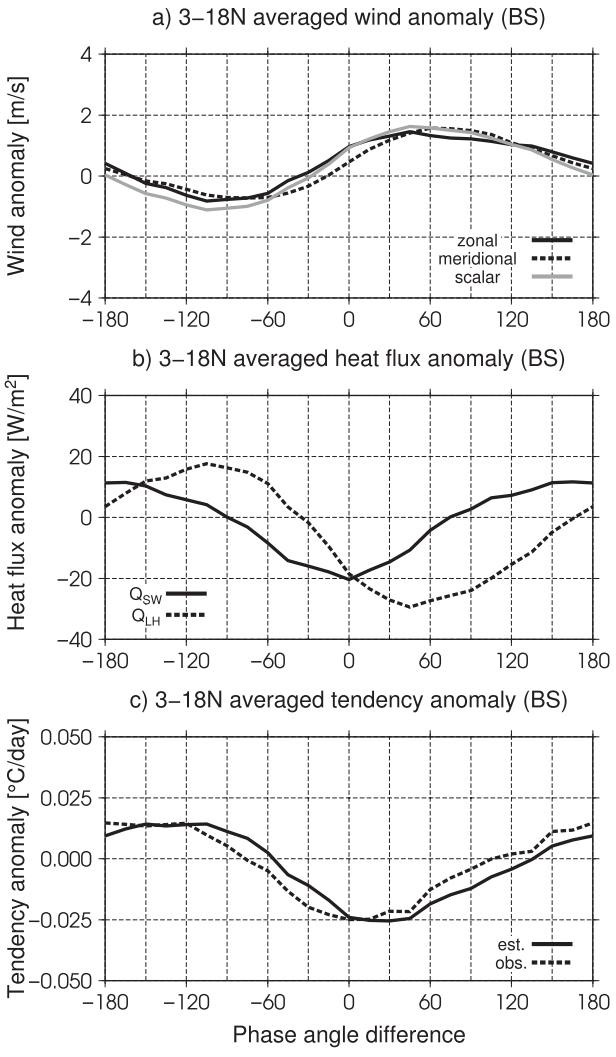

FIG. 11. Time series in terms of ISO phase angle relative to the OLR minimum for latitudinal average between 3° and 18°N in boreal summer for (a) zonal (solid black), meridional (dashed), and scalar (solid gray) winds, (b) Q_{SW} (solid) and Q_{LH} (dashed), and (c) tendency of the estimated ocean MLT (solid) and observed SST (dashed).

that a zonal gradient of SST anomaly creates a corresponding gradient of surface moist static energy and produces the convection development on the east of the convective center. Waliser et al. (1999) pointed out that the positive SST anomaly tends to reinforce the meridional convergence by comparing the difference in air–sea coupling on the simulation. They pointed out that the enhanced meridional convergence is associated with the frictional wave–convective instability of the second kind (CISK) mechanism.

An interesting implication in this study is the possibility that ISO propagation may tend to be guided into a channel of background westerlies. A basic westerly wind is located from the Indian Ocean to the Maritime Continent (Lettau 1974; Wang 1988) and shifted to the summer hemisphere. Lettau (1974) showed that overall the seasonal distribution of the basic surface westerly wind is explained by the balance between the meridional gradient of surface pressure and the Coriolis force. Lindzen and Hou (1988) pointed out that the surface westerly wind occurs over the latitudinal band between the equator and the heating center near the equator resulting from their model of the Hadley circulation. In boreal winter, meridional wind from higher latitudes converges south of the equator over the Indian Ocean. The northerly cross-equatorial flow is veered to a westerly wind by the Coriolis force in the southern narrow latitude band. The basic westerly wind extends widely to the Indian Ocean in boreal summer and northwestern Australia coast in boreal winter and is sustained by monsoon troughs over the Indian subcontinent and the Australian continent (e.g., Webster et al. 1998). The spatial distribution of the basic westerly wind is closely related with the seasonal cycle of the Hadley circulation and the monsoon circulation, which suggests that the ISO propagation paths are affected by a modulation due to the distribution of the background tropical circulations. Inness and Slingo (2003) and Inness et al. (2003) pointed out that improvement of the basic surface westerly wind simulated by the air–sea coupling model results in a better representation of the ISO.

The temporal variability of the ocean mixed layer thickness is assumed to be constant in the heat budget analysis, so that the current study does not take into account the entrainment cooling. The importance of the entrainment effect on the SST variability associated with ISOs is suggested by model studies (e.g., Li et al. 2008) and in situ observations (Drushka et al. 2012). Li et al. (2008) pointed out that the entrainment effect works in phase with shortwave and latent heat fluxes. The entrainment effect tends to be in phase with surface heat flux forcing rather than out of phase. The ocean MLT tendency estimated by the current analysis somewhat lags behind the observed SST tendency (Figs. 7c, 8c, and 11c). These lags may arise from the entrainment effect and other factors. Nevertheless, the SST tendency is overall captured by the estimated from the MLT budget analysis, which suggests that the present assumptions including the constant mixed layer depth (MLD) are verifiable to that extent.

Understanding the geographical distribution of surface winds is important for seasonality and regionalism of the SST variability associated with the ISO. Whether the SST variability is essentially important for the propagation mechanism of the ISO is beyond the current study and left for future investigations.

Acknowledgments. The authors thank the anonymous reviewers for their valuable comments and Tristan L'Ecuyer for providing the dataset from the HERB algorithm, which was generated under the support of National Aeronautics and Space Administration (NASA) Energy and Water Cycle Study (NEWS) Grant NAG06GC46G. The QSCAT SeaWinds dataset is produced by Remote Sensing Systems (http://www.remss.com). The AIRS/AMSU level 2 product was acquired as part of the activities of NASA's Science Mission Directorate and is archived and distributed by the Goddard Earth Sciences (GES) Data and Information Services Center (DISC). The OSCAR surface current product was obtained from the Physical Oceanography Distributed Active Archive Center (PODAAC) at the NASA Jet Propulsion Laboratory, Pasadena, California. SeaWiFS data were acquired from NASA's ocean color website (http://oceancolor.gsfc.nasa.gov). The OISST Climate Data Record (CDR) used in this study was acquired from NOAA's National Climatic Data Center (http://www.ncdc.noaa.gov). This CDR was originally developed by Richard Reynolds and colleagues for the NOAA's CDR program. The *WOA09* temperature data were obtained from the NOAA/National Oceanographic Data Center. The mixed layer depth dataset was downloaded online (http://www.ifremer.fr/cerweb/deboyer/mld/home.php). The Tropical Atmosphere Ocean (TAO) project office of the NOAA/ Pacific Marine Environmental Laboratory (PMEL) provided ocean buoy data. The authors thank Hatsuki Fujinami for invaluable comments and suggestions and Fumie Akimoto Furuzawa for satellite data collection and management. This work was partly supported by Japan Society for the Promotion of Science (JSPS) Grant-in-Aid for Scientific Research 26287113.

APPENDIX

Error Analysis of Satellite Data

The heat budget in the current study is estimated from various satellite data. Some key parameters of satellite estimates are compared with in situ observations. In situ data are obtained by Tropical Atmosphere Ocean (TAO) arrayed buoys, and turbulent fluxes are computed from the Coupled Ocean–Atmosphere Response Experiment (COARE) version 3.0b algorithm (Fairall et al. 2003). These data are provided by the TAO project office of the NOAA/Pacific Marine Environmental Laboratory. Parameters are surface air temperature T_a, water vapor mixing ratio $q_{v,s}$, the downwelling surface shortwave radiation (SSR) and surface longwave radiation (SLR), the latent heat flux Q_{LH}, and the sensible heat flux Q_{SH}. Satellite overpasses and arrayed buoys located between 30°E and 180° are matched up within 1.5° resolution. The sampling number depends on the existing observation for each parameter. Table A1 shows sample number, bias, root-mean-square error (RMSE), and correlation coefficient r. In situ T_a and $q_{v,s}$ are compared together with satellite estimates of the AIRX2RET product and the SL model method described in section 2. The estimations of T_a ($q_{v,s}$) used by the SL model have RMSE of 0.9°C (0.9 g kg^{-1}) and bias of −0.7°C (−0.1 g kg^{-1}). On the other hand, the accuracy of T_a ($q_{v,s}$) derived from the AIRX2RET product has RMSE of 1.3°C (1.9 g kg^{-1}) and bias of −1.1°C (−1.8 g kg^{-1}). The estimation of the SL model is higher in accuracy and smaller in bias than the AIRX2RET product. Jackson and Wick (2010) showed that the satellite retrieval RMSE of T_a is 1.6°C. Iwasaki and Kubota (2012) showed the typical accuracy of satellite derived $q_{v,s}$ in the range from 1.2 to 2.0 g kg^{-1}. The RMSEs (biases) of heat fluxes are 68.2 (36.2), 14.1 (5.7), 36.7 (−7.8), and 6.8 (−2.7) W m^{-2} for SSR, SLR, Q_{LH}, and Q_{SH}, respectively. L'Ecuyer and McGarragh (2010) showed that RMSEs of satellite instantaneous retrievals of SSR and SLR against two ocean buoys are from 87.2 to 106.1 W m^{-2} and from 28.2 to 31.9 W m^{-2}. Overestimation of satellite SSR for 36.2 W m^{-2} is also shown in L'Ecuyer and McGarragh (2010). The large bias of SSR flux may result in the climatological imbalance of heat budget, while the bias is removed by the analysis in anomaly fields. Bourras (2006) showed that the accuracy of some satellite-derived Q_{LH} is a range from 24.0 to 41.2 W m^{-2}. Compared to radiative flux and turbulent flux, the accuracy of heat fluxes associated with the oceanic internal dynamics is difficult to estimate from the in situ data and may result in additional potential uncertainty of the current analysis.

TABLE A1. Errors for each observed parameter. Number of data used, bias, RMSE, and correlation coefficient r are calculated against in situ data; "SL" indicates the estimation by the SL model and "AIRX" indicates the AIRX2RET product.

	No.	Bias	RMSE	r
SL T_a (°C)	52422	−0.70	0.93	0.633
AIRX T_a (°C)	52422	−1.13	1.34	0.534
SL $q_{v,s}$ (g kg^{-1})	52422	−0.08	0.92	0.559
AIRX $q_{v,s}$ (g kg^{-1})	52422	−1.78	1.86	0.532
SSR (W m^{-2})	31209	36.2	68.2	0.555
SLR (W m^{-2})	1571	5.68	14.1	0.793
Q_{LH} (W m^{-2})	37137	−7.82	36.7	0.725
Q_{SH} (W m^{-2})	37137	−2.68	6.77	0.511

REFERENCES

Bauer, S., M. S. Swenson, A. Griffa, A. J. Mariano, and K. Owens, 1998: Eddy-mean flow decomposition and eddy-diffusivity

estimates in the tropical Pacific Ocean: 1. Methodology. *J. Geophys. Res.,* **103** (C13), 30 855–30 871, doi:10.1029/1998JC900009.

Bonjean, F., and G. S. E. Lagerloef, 2002: Diagnostic model and analysis of the surface currents in the tropical Pacific Ocean. *J. Phys. Oceanogr.,* **32,** 2938–2954, doi:10.1175/1520-0485(2002)032<2938:DMAAOT>2.0.CO;2.

Bourras, D., 2006: Comparison of five satellite-derived latent heat flux products to moored buoy data. *J. Climate,* **19,** 6291–6313, doi:10.1175/JCLI3977.1.

Chang, P., 1993: Seasonal cycle of sea surface temperature and mixed layer heat budget in the tropical Pacific Ocean. *Geophys. Res. Lett.,* **20,** 2079–2082, doi:10.1029/93GL02374.

de Boyer Montégut, C., G. Madec, A. S. Fischer, A. Lazar, and D. Iudicone, 2004: Mixed layer depth over the global ocean: An examination of profile data and a profile-based climatology. *J. Geophys. Res.,* **109,** C12003, doi:10.1029/2004JC002378.

Drushka, K., J. Sprintall, S. T. Gille, and S. Wijffels, 2012: In situ observations of Madden–Julian oscillation mixed layer dynamics in the Indian and western Pacific Oceans. *J. Climate,* **25,** 2306–2328, doi:10.1175/JCLI-D-11-00203.1.

Duvel, J. P., and J. Vialard, 2007: Indo-Pacific sea surface temperature perturbations associated with intraseasonal oscillations of tropical convection. *J. Climate,* **20,** 3056–3082, doi:10.1175/JCLI4144.1.

Fairall, C. W., E. F. Bradley, J. E. Hare, A. A. Grachev, and J. B. Edson, 2003: Bulk parameterization of air–sea fluxes: Updates and verification for the COARE algorithm. *J. Climate,* **16,** 571–591, doi:10.1175/1520-0442(2003)016<0571:BPOASF>2.0.CO;2.

Flatau, M., P. J. Flatau, P. Phoebus, and P. P. Niiler, 1997: The feedback between equatorial convection and local radiative and evaporative processes: The implications for intraseasonal oscillations. *J. Atmos. Sci.,* **54,** 2373–2386, doi:10.1175/1520-0469(1997)054<2373:TFBECA>2.0.CO;2.

Foltz, G. R., J. Vialard, B. Praveen Kumar, and M. J. McPhaden, 2010: Seasonal mixed layer heat balance of the southwestern tropical Indian Ocean. *J. Climate,* **23,** 947–965, doi:10.1175/2009JCLI3268.1.

Gutzler, D. S., and R. A. Madden, 1989: Seasonal variations in the spatial structure of intraseasonal tropical wind fluctuations. *J. Atmos. Sci.,* **46,** 641–660, doi:10.1175/1520-0469(1989)046<0641:SVITSS>2.0.CO;2.

Hendon, H. H., 2012: Air–sea interaction. *Intraseasonal Variability in the Atmosphere–Ocean Climate System,* 2nd ed., W. K. Lau and D. E. Waliser, Eds., Springer, 247–270.

——, and B. Liebmann, 1990: The intraseasonal (30–50 day) oscillation of the Australian summer monsoon. *J. Atmos. Sci.,* **47,** 2909–2924, doi:10.1175/1520-0469(1990)047<2909:TIDOOT>2.0.CO;2.

——, and J. Glick, 1997: Intraseasonal air–sea interaction in the tropical Indian and Pacific Oceans. *J. Climate,* **10,** 647–661, doi:10.1175/1520-0442(1997)010<0647:IASIIT>2.0.CO;2.

Inness, P. M., and J. M. Slingo, 2003: Simulation of the Madden-Julian oscillation in a coupled general circulation model. Part I: Comparison with observations and an atmosphere-only GCM. *J. Climate,* **16,** 345–364, doi:10.1175/1520-0442(2003)016<0345:SOTMJO>2.0.CO;2.

——, ——, E. Guilyardi, and J. Cole, 2003: Simulation of the Madden-Julian oscillation in a coupled general circulation model. Part II: The role of the basic state. *J. Climate,* **16,** 365–382, doi:10.1175/1520-0442(2003)016<0365:SOTMJO>2.0.CO;2.

Iwasaki, S., and M. Kubota, 2012: Algorithms for estimation of air-specific humidity using TMI data. *Int. J. Remote Sens.,* **33,** 7413–7430, doi:10.1080/01431161.2012.685974.

Jackson, D. L., and G. A. Wick, 2010: Near-surface air temperature retrieval derived from AMSU-A and sea surface temperature observations. *J. Atmos. Oceanic Technol.,* **27,** 1769–1776, doi:10.1175/2010JTECHA1414.1.

Kanemaru, K., and H. Masunaga, 2013: A satellite study of the relationship between sea surface temperature and column water vapor over tropical and subtropical oceans. *J. Climate,* **26,** 4204–4218, doi:10.1175/JCLI-D-12-00307.1.

Kemball-Cook, S., and B. Wang, 2001: Equatorial waves and air–sea interaction in the boreal summer intraseasonal oscillation. *J. Climate,* **14,** 2923–2942, doi:10.1175/1520-0442(2001)014<2923:EWAASI>2.0.CO;2.

——, ——, and X. Fu, 2002: Simulation of the intraseasonal oscillation in the ECHAM-4 model: The impact of coupling with an ocean model. *J. Atmos. Sci.,* **59,** 1433–1453, doi:10.1175/1520-0469(2002)059<1433:SOTIOI>2.0.CO;2.

Klingaman, N. P., H. Weller, J. M. Slingo, and P. M. Inness, 2008: The intraseasonal variability of the Indian summer monsoon using TMI sea surface temperatures and ECMWF reanalysis. *J. Climate,* **21,** 2519–2539, doi:10.1175/2007JCLI1850.1.

Krishnamurti, T. N., and D. Subrahmanyam, 1982: The 30–50 day mode at 850 mb during MONEX. *J. Atmos. Sci.,* **39,** 2088–2095, doi:10.1175/1520-0469(1982)039<2088:TDMAMD>2.0.CO;2.

Lagerloef, G. S. E., G. T. Mitchum, R. B. Lukas, and P. P. Niiler, 1999: Tropical Pacific near-surface currents estimated from altimeter, wind, and drifter data. *J. Geophys. Res.,* **104** (C10), 23 313–23 326, doi:10.1029/1999JC900197.

Large, W., J. McWilliams, and S. Doney, 1994: Oceanic vertical mixing: A review and a model with a nonlocal boundary layer parameterization. *Rev. Geophys.,* **32,** 363–403, doi:10.1029/94RG01872.

Lau, K.-M., and C.-H. Sui, 1997: Mechanisms of short-term sea surface temperature regulation: Observations during TOGA COARE. *J. Climate,* **10,** 465–472, doi:10.1175/1520-0442(1997)010<0465:MOSTSS>2.0.CO;2.

L'Ecuyer, T. S., and G. L. Stephens, 2003: The tropical oceanic energy budget from the TRMM Perspective. Part I: Algorithm and uncertainties. *J. Climate,* **16,** 1967–1985, doi:10.1175/1520-0442(2003)016<1967:TTOEBF>2.0.CO;2.

——, and G. McGarragh, 2010: A 10-year climatology of tropical radiative heating and its vertical structure from TRMM observations. *J. Climate,* **23,** 519–541, doi:10.1175/2009JCLI3018.1.

Lettau, B., 1974: Pressure–wind relationships in the equatorial surface westerlies. *Mon. Wea. Rev.,* **102,** 208–218, doi:10.1175/1520-0493(1974)102<0208:PWRITE>2.0.CO;2.

Li, T., F. Tam, X. Fu, Z. Tian-Jun, and Z. Wei-Jun, 2008: Causes of the intraseasonal SST variability in the tropical Indian Ocean. *Atmos. Oceanic Sci. Lett.,* **1,** 18–23.

Lindzen, R. S., and A. V. Hou, 1988: Hadley circulations for zonally averaged heating centered off the equator. *J. Atmos. Sci.,* **45,** 2416–2427, doi:10.1175/1520-0469(1988)045<2416:HCFZAH>2.0.CO;2.

Locarnini, R. A., A. V. Mishonov, J. I. Antonov, T. P. Boyer, H. E. Garcia, O. K. Baranova, M. M. Zweng, and D. R. Johnson, 2010: *Temperature.* Vol. 1, *World Ocean Atlas 2009,* NOAA Atlas NESDIS 68, 184 pp.

Madden, R. A., 1986: Seasonal variations of the 40–50 day oscillation in the tropics. *J. Atmos. Sci.,* **43,** 3138–3158, doi:10.1175/1520-0469(1986)043<3138:SVOTDO>2.0.CO;2.

——, and P. R. Julian, 1971: Detection of a 40–50 day oscillation in the zonal wind in the tropical Pacific. *J. Atmos. Sci.,* **28,** 702–708, doi:10.1175/1520-0469(1971)028<0702:DOADOI>2.0.CO;2.

——, and ——, 1972: Description of global-scale circulation cells in the tropics with a 40–50 day period. *J. Atmos. Sci.,* **29,** 1109–1123, doi:10.1175/1520-0469(1972)029<1109:DOGSCC>2.0.CO;2.

Masunaga, H., and T. S. L'Ecuyer, 2010: The southeast Pacific warm band and double ITCZ. *J. Climate,* **23,** 1189–1208, doi:10.1175/2009JCLI3124.1.

——, and ——, 2011: Equatorial asymmetry of the east Pacific ITCZ: Observational constraints on the underlying processes. *J. Climate,* **24,** 1784–1800, doi:10.1175/2010JCLI3854.1.

Matthews, A. J., B. J. Hoskins, J. M. Slingo, and M. Blackburn, 1996: Development of convection along the SPCZ within a Madden–Julian oscillation. *Quart. J. Roy. Meteor. Soc.,* **122,** 669–688, doi:10.1002/qj.49712253106.

Morel, A., and D. Antoine, 1994: Heating rate within the upper ocean in relation to its bio-optical state. *J. Phys. Oceanogr.,* **24,** 1652–1665, doi:10.1175/1520-0485(1994)024<1652:HRWTUO>2.0.CO;2.

Nakazawa, T., 1995: Intraseasonal oscillations during the TOGA-COARE IOP. *J. Meteor. Soc. Japan,* **73,** 305–319.

O'Reilly, J., and Coauthors, 2000: SeaWiFS postlaunch calibration and validation analyses, Part 3. NASA Tech. Memo. 2000-206892, Vol. 11, S. B. Hooker and E. R. Firestone, Eds., NASA Goddard Space Flight Center, 49 pp.

Reynolds, R. W., T. M. Smith, C. Liu, D. B. Chelton, K. S. Casey, and M. G. Schlax, 2007: Daily high-resolution-blended analyses for sea surface temperature. *J. Climate,* **20,** 5473–5496, doi:10.1175/2007JCLI1824.1.

Ricciardulli, L., and F. Wentz, 2011: Reprocessed QuikSCAT (V04) wind vectors with Ku-2011 geophysical model function. Remote Sensing Systems Tech. Rep. 43011, 8 pp. [Available online at images.remss.com/qscat/qscat_Ku2011_tech_report.pdf.]

Salby, M. L., and H. H. Hendon, 1994: Intraseasonal behavior of clouds, temperature, and motion in the tropics. *J. Atmos. Sci.,* **51,** 2207–2224, doi:10.1175/1520-0469(1994)051<2207:IBOCTA>2.0.CO;2.

Sengupta, D., B. N. Goswami, and R. Senan, 2001: Coherent intraseasonal oscillations of ocean and atmosphere during the Asian summer monsoon. *Geophys. Res. Lett.,* **28,** 4127–4130, doi:10.1029/2001GL013587.

Shinoda, T., H. H. Hendon, and J. Glick, 1998: Intraseasonal variability of surface fluxes and sea surface temperature in the tropical western Pacific and Indian Oceans. *J. Climate,* **11,** 1685–1702, doi:10.1175/1520-0442(1998)011<1685:IVOSFA>2.0.CO;2.

Susskind, J., C. Barnet, and J. Blaisdell, 2003: Retrieval of atmospheric and surface parameters from AIRS/AMSU/HSB data in the presence of clouds. *IEEE Trans. Geosci. Remote Sens.,* **41,** 390–409, doi:10.1109/TGRS.2002.808236.

——, J. Blaisdell, L. Iredell, and F. Keita, 2011: Improved temperature sounding and quality control methodology using AIRS/AMSU data: The AIRS Science Team version 5 retrieval algorithm. *IEEE Trans. Geosci. Remote Sens.,* **49,** 883–907, doi:10.1109/TGRS.2010.2070508.

Vialard, J., G. R. Foltz, M. J. McPhaden, J. P. Duvel, and C. de Boyer Montégut, 2008: Strong Indian Ocean sea surface temperature signals associated with the Madden–Julian Oscillation in late 2007 and early 2008. *Geophys. Res. Lett.,* **35,** L19608, doi:10.1029/2008GL035238.

Waliser, D. E., K. M. Lau, and J.-H. Kim, 1999: The influence of coupled sea surface temperatures on the Madden-Julian oscillation: A model perturbation experiment. *J. Atmos. Sci.,* **56,** 333–358, doi:10.1175/1520-0469(1999)056<0333:TIOCSS>2.0.CO;2.

Wang, B., 1988: Comments on ''An air–sea interaction model of intraseasonal oscillation in the tropics.'' *J. Atmos. Sci.,* **45,** 3521–3525, doi:10.1175/1520-0469(1988)045<3521:COAIMO>2.0.CO;2.

——, and H. Rui, 1990: Synoptic climatology of transient tropical intraseasonal convection anomalies: 1975–1985. *Meteor. Atmos. Phys.,* **44,** 43–61, doi:10.1007/BF01026810.

——, and X. Xie, 1998: Coupled modes of the warm pool climate system. Part I: The role of air–sea interaction in maintaining Madden–Julian oscillation. *J. Climate,* **11,** 2116–2135, doi:10.1175/1520-0442-11.8.2116.

Wang, W., and M. J. McPhaden, 1999: The surface-layer heat balance in the equatorial Pacific Ocean. Part I: Mean seasonal cycle. *J. Phys. Oceanogr.,* **29,** 1812–1831, doi:10.1175/1520-0485(1999)029<1812:TSLHBI>2.0.CO;2.

Webster, P. J., V. O. Magaña, T. N. Palmer, J. Shukla, R. A. Tomas, M. Yanai, and T. Yasunari, 1998: Monsoons: Processes, predictability, and the prospects for prediction. *J. Geophys. Res.,* **103** (C7), 14 451–14 510, doi:10.1029/97JC02719.

Wheeler, M. C., and H. H. Hendon, 2004: An all-season real-time multivariate MJO Index: Development of an index for monitoring and prediction. *Mon. Wea. Rev.,* **132,** 1917–1932, doi:10.1175/1520-0493(2004)132<1917:AARMMI>2.0.CO;2.

Woolnough, S. J., J. M. Slingo, and B. J. Hoskins, 2000: The relationship between convection and sea surface temperature on intraseasonal timescales. *J. Climate,* **13,** 2086–2104, doi:10.1175/1520-0442(2000)013<2086:TRBCAS>2.0.CO;2.

——, F. Vitart, and M. A. Balmaseda, 2007: The role of the ocean in the Madden–Julian oscillation: Implications for MJO prediction. *Quart. J. Roy. Meteor. Soc.,* **133,** 117–128, doi:10.1002/qj.4.

Yasunari, T., 1979: Cloudiness fluctuations associated with the Northern Hemisphere summer monsoon. *J. Meteor. Soc. Japan,* **57,** 227–242.

——, 1980: A quasi-stationary appearance of 30 to 40 day period in the cloudiness fluctuations during the summer monsoon over India. *J. Meteor. Soc. Japan,* **58,** 225–229.

Zhang, C., and M. Dong, 2004: Seasonality in the Madden–Julian oscillation. *J. Climate,* **17,** 3169–3180, doi:10.1175/1520-0442(2004)017<3169:SITMO>2.0.CO;2.